Accurate numerical simulation of radiative transfer with application to crystal growth

Alexandre Ern [a] Jean-Luc Guermond [b]

[a] *CERMICS, Ecole Nationale des Ponts et Chaussées, 6 et 8 avenue Blaise Pascal, 77455 Marne la Vallée cedex 2, France*

[b] *LIMSI, CNRS, BP133, 91403 Orsay cedex, France*

Abstract

We present a mathematical formulation and a numerical investigation of a thermomagnetic problem arising in crystal growth applications. The governing equations are the quasi-static, time harmonic, axisymmetric Maxwell equations coupled with an energy conservation equation. Multiple reflection radiant energy transfer is modeled by an integral equation yielding a strongly nonlinear and nonlocal problem. Key issue is the accurate and cost effective evaluation of the multiple reflection radiation flux. The present method uses a discontinuous Galerkin method with local azimuthal refinement near shadowing obstacles and an appropriate renormalization of the view factor matrix which guarantees mathematically under some assumptions that the discrete problem is well posed. Numerical results are presented for reactors with simple geometry where the solution is compared to previous numerical work and for an industrial prototype involving several nonconvex radiating surfaces.

Key words: Finite elements, discontinuous Galerkin, grey body radiation, crystal growth

1 Introduction

During the last decade, silicon carbide (SiC) has sparked extensive interest in the semiconductor industry. Indeed, important advances have been accomplished in the manufacturing of high power and high temperature SiC based optoelectronic devices. However, one crucial step still restricting the industrial production of SiC devices is the scarce availability of single crystal SiC wafers with a high enough level of crystalline perfection in terms of micropipe and dislocation density. Such wafers are commonly grown using a modified Lely method (see e.g. [18] for a review). Growth takes place inside a radiofrequency (RF) heated graphite crucible with a single crystalline seed fixed at the top

and SiC powder placed at the bottom. The thermal gradient in the growth cavity must be controlled in such a way that sublimation occurs in the powder and deposition on the crystal seed. Typical temperature gradients are of the order of 100 Kcm^{-1}. Temperatures range between 2300 and 3000 K in the crucible and between 2700 and 2800 K in the crystal seed.

Equipment design and operating parameters for wafer production have been steadily improved over the years mainly by engineers' experimental knowledge of the growth process. More recently, numerical modeling has emerged as an additional tool complementing experimental results and providing valuable insight into the physical and chemical phenomena involved inside the crucible. Several research groups have developed comprehensive numerical models accounting for magnetic, thermal and chemical phenomena (see, among others, [1,3,11,13,17]). A recent state of the art review [10] indicates that thermomagnetic coupled with simplified chemical modeling has reached a certain level of maturity while detailed knowledge of surface processes and defect formation still challenges the research community. Current research developments in numerical modeling include among others optimal control techniques to improve crucible design [7], impact of source material on growth conditions [21] and thermoelastic stresses in the bulk crystal and their correlation to defect formation [16].

The goal of this paper is to focus on the part of the model which has reached maturity (the thermomagnetic problem) and to derive an accurate and stable numerical method to calculate the temperature distribution inside a crucible with multiple reflection radiant energy transfer in a complex geometry. Its main contribution is thus to yield a robust methodology for thermomagnetic modeling to be ultimately coupled with more comprehensive chemical and thermomechanical models. The emphasis on the thermomagnetic problem is strongly motivated by the fact that temperature gradient control around the crystal seed is a key issue in product quality. Radiative heat transfer has been extensively dealt with in the crystal growth literature. However, to the authors' knowledge, the radiation problem has always been considered only in its discrete form. In these approaches, the radiant surface is divided into a finite number of cells and configuration factors (or view factors) need to be evaluated for all the cell couples. For simple geometries, the configuration factors can be evaluated analytically using tabulated values and classical view factor algebra [4,5]. In most practical cases, a numerical evaluation is needed, as detailed for instance in [6]. The methodology derived in the present paper is based on the continuous formulation of the radiation problem through an integral equation. An approximate integral equation is derived using a discontinuous Galerkin method and Gaussian quadrature. Besides accuracy and stability, another important advantage of the method is its compatibility with the finite element formulation of the global conservation equations since it yields the discrete radiation flux at the quadrature nodes. Further-

more, the computational costs are reduced significantly by local refinement in the azimuthal direction in the neighborhood of shadowing obstacles. Finally, introducing an appropriate renormalization of the view matrix, we establish under some assumptions the existence of a solution to the discrete problem.

This paper is organized as follows. In the next section, we formulate mathematically the governing equations. The numerical method is described and analyzed in section 3. Finally, in section 4 we present numerical results assessing both accuracy and computational efficiency of the proposed method.

2 Problem Formulation

2.1 Physical modeling

A schematic representation of a crystal growth reactor with idealized geometry is presented in Figure 1. A graphite crucible coated with an insulating foam contains the SiC powder and the growth cavity. A RF source current is imposed in the induction coils. The conductive materials (graphite, foam and SiC powder) are heated by the inductive currents through Joule's effect. The temperature distribution inside the growth reactor results from a balance between conductive and radiative heat transfer with multiple reflections occurring inside the growth cavity. Convective heat transfer inside the cavity may be neglected for typical operating conditions [3,11].

The three-dimensional electromagnetic field is modeled by the Maxwell equations with some simplifying assumptions. First, we assume that the electromagnetic field is time harmonic with angular velocity ω and frequency f. In addition, for low frequency eddy current problems (with f typically lower than 1 Mhz), the displacement currents may be neglected leading to the quasi-static approximation. Finally, we restrict ourselves to axisymmetric configurations with (r, z) denoting the radial and axial coordinates respectively. With these assumptions, the Maxwell equations reduce to

$$\begin{cases} \mathrm{rot}\left(\frac{1}{\mu}\,\mathrm{rot}^*\, A\right) = j \\ \qquad \mathtt{i}\omega A + E = 0 \end{cases}$$

with $\mathrm{rot}^*\, A = (-\partial_z A, \frac{1}{r}\partial_r(rA))$ and $\mathtt{i}^2 = -1$. Here, A and E are scalar fields denoting the magnetic potential and the azimuthal component of the electric field respectively, μ is the magnetic permeability and j the current density.

The induction coils are modeled by imposing the current density to a prescribed value. This approximation is classical in this context. Since the current

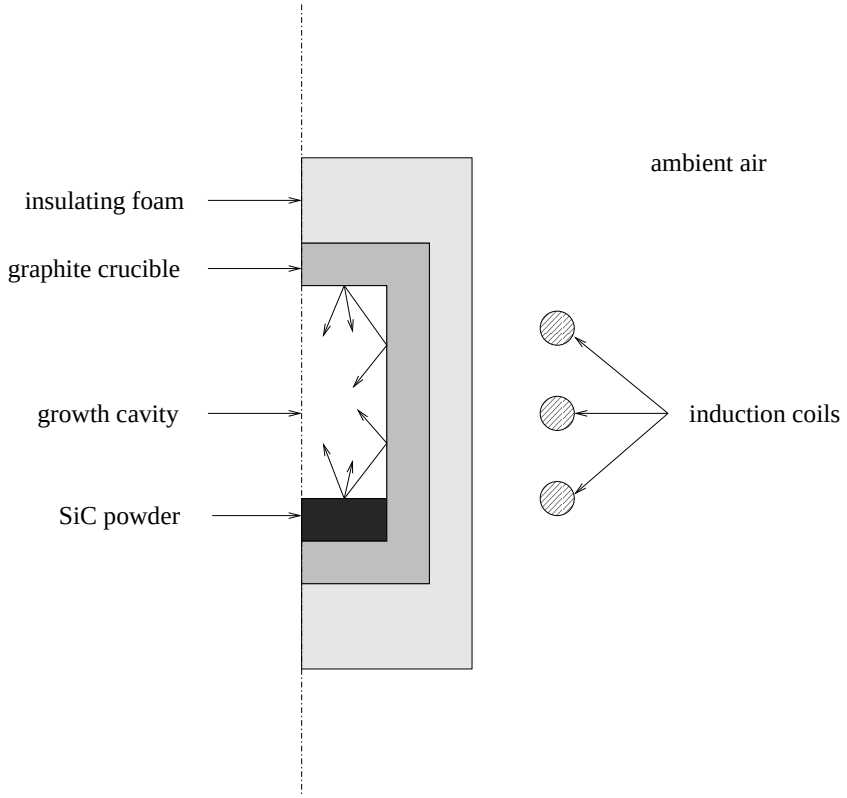

Fig. 1. Schematic representation of a crystal growth reactor with idealized geometry.

density is not constant is space through the induction coils, the actual section of the coils are replaced by equivalent sections in the model [11]. In the other conducting media, we assume Ohm's law $j = \sigma E$ where σ is the (temperature dependent) electric conductivity. Upon formally setting the electric conductivity to zero in the induction coils, we may write an equation valid in the whole space which reads

$$\mathrm{rot}\left(\tfrac{1}{\mu}\,\mathrm{rot}^{*}\,A\right) + \mathtt{i}\sigma\omega A = J_d, \tag{1}$$

where J_d is zero everywhere except in the induction coils where it takes a specified value.

The inductive currents in conductive media yield a volumetric heat release through Joule dissipation in the form $Q = \frac{1}{2}\sigma\omega^2|A|^2$. Diffusive heat balance inside the various materials thus reads

$$-\,\mathrm{div}\,(k(T)\nabla T) = \tfrac{1}{2}\sigma\omega^2|A|^2, \tag{2}$$

where $k(T)$ is the (temperature dependent) thermal conductivity.

An important aspect of energy balance in the growth cavity is radiant energy transfer including emission, reflection and adsorption. Radiant surfaces are assumed to behave like grey bodies (i.e., the radiative exchanges are indepen-

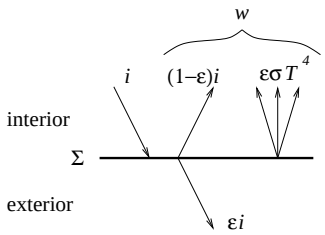

Fig. 2. Radiant energy transfer with reflection.

dent of the wavelength) and are characterized by an emissivity coefficient ε [4]. We also assume that the radiant surfaces are separated by non participating media, i.e. that the gases inside the cavity do not affect radiant energy transfers.

In a *nonconvex* cavity, three-dimensional effects arise since couples of points may not see each other depending on their respective azimuthal position. We will denote by Σ the radiant surface in the three-dimensional physical space and by Σ_m its meridian in the (r, z) plane. On a given point in Σ, let T be the temperature and i the incident flux of radiant energy. A fraction of it, εi, is transmitted towards the exterior of the cavity and the remaining part, $(1-\varepsilon)i$, is reflected back towards the interior (see figure 2). As a result, the radiosity, defined as the total flux of radiant energy leaving Σ towards the interior, reads

$$w = (1 - \varepsilon)i + \varepsilon\sigma T^4, \tag{3}$$

where $\sigma = 5.67\times10^{-8}$ $\mathrm{Wm^{-2}K^{-4}}$ is the Stefan-Boltzmann constant. Furthermore, the incident energy flux is related to the radiosity by Lambert's law in the form

$$i = Fw. \tag{4}$$

Here, we have introduced the integral operator $F : L^p(\Sigma) \to L^p(\Sigma) \to (1 \leq p \leq \infty)$ defined as

$$Fu(x) = \int_\Sigma f(x, y)\, u(y)\, dy, \quad \forall x \in \Sigma.$$

The integral kernel reads

$$f(x, y) = \mathcal{V}(x, y)\, \Xi(x, y), \quad x, y \in \Sigma,$$

where

$$\mathcal{V}(x, y) = \frac{1}{\pi} \frac{n_x{\cdot}(x - y)\; n_y{\cdot}(y - x)}{\|x - y\|^4},$$

n_x and n_y are the outward normal to Σ at x and y respectively and

$$\Xi(x, y) = \begin{cases} 1 & \text{if the points } x \text{ and } y \text{ see each other,} \\ 0 & \text{otherwise.} \end{cases}$$

The integral kernel f satisfies the following two important properties of symmetry and normalization:

$$f(x,y) = f(y,x), \ \ \forall x, y \in \Sigma \qquad \text{and} \qquad \int_\Sigma f(x,y)\, dy = 1, \ \ \forall x \in \Sigma.$$

In the sequel, it will be convenient to introduce the total energy flux from the exterior to the interior of the cavity. This flux, denoted by Φ, satisfies the integral equation

$$\tfrac{1}{\varepsilon}\Phi - F\left(\tfrac{1-\varepsilon}{\varepsilon}\Phi\right) = \sigma T^4 - F(\sigma T^4).$$

From the properties of the kernel f, we readily deduce that

$$\begin{cases} (\sigma T^4 \text{ constant over } \Sigma) \Longrightarrow (\Phi = 0 \text{ over } \Sigma) \\ \forall T, \ \ \int_\Sigma \Phi = 0. \end{cases}$$

Energy balance between radiant and diffusive transfer may then be expressed as

$$[k\nabla T]\cdot n_\Sigma = \Phi \quad \text{over } \Sigma, \tag{5}$$

where n_Σ denotes the outward normal to Σ and $[k\nabla T]\cdot n_\Sigma$ the difference between exterior and interior values.

The magnetic and thermal problems are posed on different domains. Referring to figure 1, subdomain Ω_1 denotes the SiC powder, Ω_2 the growth cavity, Ω_3 the graphite crucible, Ω_4 the insulating foam, Ω_5 the induction coils and Ω_6 the ambient air. The magnetic problem is then posed over $\Omega^A = \Omega_1 \cup \ldots \cup \Omega_6$ and the thermal problem over $\Omega^T = \Omega_1 \cup \ldots \cup \Omega_4$. Boundary conditions for the magnetic problem impose $A = 0$ on the symmetry axis and far enough from the induction coils. On the other hand, boundary conditions for the temperature may take various forms. Introducing the decomposition $\partial\Omega^T = \Gamma_d \cup \Gamma_n \cup \Gamma_e$, we consider a Dirichlet condition $T = T_d$ on Γ_d, an homogeneous Neumann on Γ_n (typically the symmetry axis) and a detailed radiative, convective and diffusive energy balance on Γ_e in the form

$$k(T)\nabla T\cdot n_e + \eta(T - T_\infty) + \varepsilon\sigma(T^4 - T_\infty^4) = 0, \tag{6}$$

where n_e is the outward normal to Γ_e, T_∞ the ambient air temperature and η an empirical heat transfer coefficient.

In weak form, the governing equations read

$$\left\{\begin{array}{l} \text{Find } A \in V^A, \\ \int_{\Omega^A} \frac{1}{\mu}(\frac{1}{r}\partial_r(rA_r)\partial_r(r\zeta_r) + r\partial_z A_z \partial_z \zeta_z)\, drdz + \mathtt{i}\omega \int_{\Omega^A} \sigma(T) A \cdot \zeta\, rdrdz \\ = \int_{\Omega^A} J_d \cdot \zeta\, rdrdz, \qquad \forall \zeta \in V^A, \end{array}\right. \tag{7}$$

and

$$\left\{\begin{array}{l} \text{Find } T \in V^T_{T_d}, \\ \int_{\Omega^T} k(T)\nabla T \cdot \nabla \Theta\, rdrdz + \int_{\Sigma_m} \Phi(T)\,\Theta\, rdl + \int_{\Gamma_e} (\eta T + \varepsilon\sigma\Psi(T))\Theta\, rdl \\ = \int_{\Omega^T} \frac{1}{2}\sigma\omega^2 |A|^2 \Theta\, rdrdz + \int_{\Gamma_e} (\eta T_\infty + \varepsilon\sigma\Psi(T_\infty))\Theta\, rdl, \qquad \forall \Theta \in V^T_0, \end{array}\right. \tag{8}$$

where V^A and V^T_g are suitable functional spaces described below. The integral equation giving the flux Φ is rewritten as

$$\tfrac{1}{\varepsilon}\Phi - F\left(\tfrac{1-\varepsilon}{\varepsilon}\Phi\right) = \sigma\Psi(T) - F(\sigma\Psi(T)) \quad \text{with} \quad \Psi(T) = |T|^3\, T. \tag{9}$$

With such modification, it is straightforward to check using Hölder's inequality and the fact that $\|F\|_{L^p(\Sigma_m)} \leq 1$ that $\int_{\Sigma_m} \Phi(T)\, T\, rdl \geq 0$. Note also that multiple solutions of (8) may be constructed when T^4 is not replaced by $\Psi(T)$ [15].

For the magnetic problem, one may take the Hilbert space $V^A = H^1_0(\Omega^A)^2$. For the thermal problem, one may consider the affine space

$$V^T_g = \left\{\, T \in H^1(\Omega^T),\, T_{|\Sigma_m} \in L^5(\Sigma_m),\, T_{|\Gamma_d} = g \,\right\}.$$

Indeed, assuming $T \in V^T_g$, one easily shows that the integral equation (9) admits a unique solution $\Phi \in L^{5/4}(\Sigma_m)$ so that the surface integral $\int_{\Sigma_m} \Phi(T)\,\Theta\, rdl$ is well defined owing to Hölder's inequality [19,20]. Problems (7) and (8) are coupled together through the temperature dependence of the electric conductivity. Problem (8) is strongly nonlinear and nonlocal. From a mathematical viewpoint, existence and uniqueness of its solution is still an open problem which will not be further investigated in this paper. Difficulties arise for closed interior cavities with radiant energy transfer over their whole boundary for which the norm of the associated integral operator is equal to one. Existence and uniqueness can be proved when the temperature is fixed on part of the radiant boundary [8,9] or when the existence of suitable super and subsolutions can be established a priori [19,20].

Remark. In the special case of temperature independent electric conductivities, the thermomagnetic problem simplifies into a two step resolution: first, a *linear* magnetic problem yielding the magnetic potential A; second, a strongly nonlinear and nonlocal problem for the temperature T.

3 Numerical Methodology

The numerical method derived in this work involves finite element discretization of the partial differential equations (PDEs), a discontinuous Galerkin approximation to the integral equation, an accurate three-dimensional ray method with local azimuthal refinement near shadowing obstacles to evaluate the view factors for complex nonconvex geometries and a Newton's method embedded in a fixed point iteration to handle the nonlinearities in the temperature equation and the thermomagnetic coupling respectively.

3.1 Finite element approximation

The domain for the magnetic problem is truncated at a finite radius R and is denoted by Ω_R^A. Given a triangulation of Ω_R^A and Ω^T, we consider linear simplicial continuous finite element spaces for the magnetic potential and the temperature denoted by V_{hR}^A and V_h^T. The Galerkin approximation reads

$$\begin{cases} \text{Find } A_h \in V_{hR}^A, \\ \int_{\Omega_R^A} \frac{1}{\mu}(\frac{1}{r}\partial_r(rA_{hr})\partial_r(r\zeta_{hr}) + r\partial_z A_{hz}\partial_z\zeta_{hz})\,drdz + \mathtt{i}\omega \int_{\Omega_R^A} \sigma(T_h)A_h\cdot\zeta_h\, rdrdz \\ = \int_{\Omega_R^A} J_d\cdot\zeta_h\, rdrdz, \qquad \forall \zeta_h \in V_{hR}^A, \end{cases} \tag{10}$$

and

$$\begin{cases} \text{Find } T_h \in V_{T_d h}^T, \\ \int_{\Omega^T} k(T_h)\nabla T_h\cdot\nabla\Theta_h\, rdrdz + \int_{\Sigma_m}\Phi_h(T_h)\,\Theta_h\, rdl + \int_{\Gamma_e}(\eta T_h + \varepsilon\sigma\Psi(T_h))\Theta_h\, rdl \\ = \int_{\Omega^T}\frac{1}{2}\sigma\omega^2|A_h|^2\Theta_h\, rdrdz + \int_{\Gamma_e}(\eta T_\infty + \varepsilon\sigma\Psi(T_\infty))\Theta_h\, rdl, \qquad \forall\Theta_h \in V_{0h}^T. \end{cases} \tag{11}$$

Volume (resp. surface) integrals are evaluated with a numerical quadrature involving 3 (resp. 2) Gauss points. The numerical evaluation of the multiple reflection radiative flux $\Phi_h(T_h)$ is discussed in the next section.

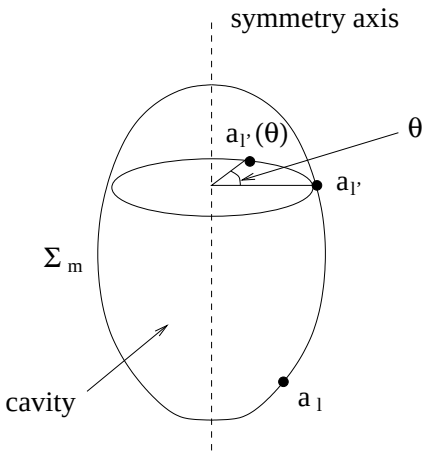

Fig. 3. Azimuthal integration of view factors.

3.2 Approximate integral equation

The triangulation of Ω^T induces a mesh of the meridian Σ_m. We use a discontinuous Galerkin method of degree one to discretize the integral equation and evaluate the discontinuous piecewise linear function Φ_h. If two Gauss points per element of Σ_m are used to approximate all the integrals, the resulting problem is equivalent to a collocation method at the Gauss points, the unknown being the value of Φ_h at those points. Note that the formalism can be readily extended to approximations of higher degree while the zero degree method where Φ_h is approximated by a piecewise constant function corresponds to the method usually reported in the engineering literature (see for instance [1,6]).

Let n_g be the total number of Gauss points on Σ_m and a_l be the lth Gauss point. Set $\omega_l = \lambda_l r_l/2$ where λ_l is the length of the segment where a_l is located and r_l the radial coordinate of a_l. Upon introducing the view matrix $F \in \mathbb{R}^{n_g,n_g}$ with coefficients

$$F_{ll'} = f_{axi}(a_l, a_{l'})\omega_{l'}, \qquad f_{axi}(a_l, a_{l'}) = 2\int_0^\pi f\Big(a_l, a_{l'}(\theta)\Big)\, d\theta,$$

the vector $\Phi_h \in \mathbb{R}^{n_g}$ with components $\Phi_{hl} = \Phi_h(a_l)$ and the vector $b \in \mathbb{R}^{n_g}$ with components $b_l = \sigma\Psi(T(a_l))$, we obtain the linear system

$$\mathrm{diag}(\tfrac{1}{\varepsilon})\Phi_h - F\left(\mathrm{diag}(\tfrac{1-\varepsilon}{\varepsilon})\Phi_h\right) = (I - F)b, \tag{12}$$

where I is the identity matrix, $\mathrm{diag}(\frac{1}{\varepsilon})_{ll'} = \frac{1}{\varepsilon(a_l)}\delta_{ll'}$, $\mathrm{diag}(\frac{1-\varepsilon}{\varepsilon})_{ll'} = \frac{1-\varepsilon(a_l)}{\varepsilon(a_l)}\delta_{ll'}$ and $\delta_{ll'}$ the Kronecker delta. Note that we have taken advantage of axial symmetry by averaging f over the azimuthal coordinate. Three-dimensional effects still arise in the actual computation of f_{axi} as detailed in the next section.

Besides its accuracy and stability properties, the discontinuous Galerkin method offers the important advantage that it yields directly the quantities $\Phi_h(a_l)$,

$1 \leq l \leq n_g$, which are needed to evaluate the surface integral $\int_{\Sigma_m} \Phi_h(T_h)\,\Theta_h$ in (8). Note also that discontinuous Galerkin is a natural way to discretize the integral equation which from a mathematical viewpoint is posed on the Banach space $L^{5/4}(\Sigma_m)$ where no continuity assumptions can be made a priori.

Because of the numerical quadratures involved, the quantities

$$S_l = \sum_{l'=1}^{n_g} F_{ll'},$$

may differ from unity. Indeed, we have

$$S_l = \sum_{l'=1}^{n_g} f_{axi}(a_l, a_{l'})\omega_{l'} \simeq \int_{\Sigma_m} f_{axi}(a_l, y)\,dy = \int_{\Sigma} f(a_l, z)\,dz = 1.$$

If the radiating surface is smooth, S_l converges to unity with third order in h because the truncation error is fourth order on each segment, two Gauss points being used locally. However, if corners are present, singularities may arise. Specifically, for a given $x \in \Sigma$, the function $f_x : z \mapsto f(x,z)$ is discontinuous when z passes through a corner that can be seen from x and has a $\frac{1}{\|x-z\|^2}$ singularity if x is located at a *convex* corner where the two neighboring edges see each other. As a result, when a convex corner is present, S_l does not converge to unity if a_l is located next to a convex corner and converges to unity with first order otherwise.

It may then be interesting to introduce a renormalization of the view matrix. Upon setting

$$G_{ll'} = \frac{1}{S_l} F_{ll'},$$

and introducing the vectors U and $W \in \mathbb{R}^{n_g}$ with components $U = (1, \ldots, 1)$ and $W = (\omega_1 S_1, \ldots, \omega_{n_g} S_{n_g})$, one readily sees that

$$GU = U \qquad \text{and} \qquad G^t W = W.$$

Therefore, the solution Φ_h of the rescaled linear system

$$\mathrm{diag}(\tfrac{1}{\varepsilon})\Phi_h - G\left(\mathrm{diag}(\tfrac{1-\varepsilon}{\varepsilon})\Phi_h\right) = (I - G)b, \tag{13}$$

satisfies the following two properties, which are important from a physical viewpoint:

- $(b \in \mathbb{R}U) \Longrightarrow (\Phi_h = 0)$ since $GU = U$;
- approximate overall conservation of radiant energy over Σ_m in the form

$$\int_{\Sigma_m} \Phi_h \simeq \sum_{l=1}^{n_g} \omega_l S_l\, \Phi_{hl} = 0,$$

since $G^t W = W$.

Other renormalizations may be considered as for instance a single modification of the largest coefficient [6]. The present renormalization offers the advantage to ensure *both* physical properties above. However, the fundamental advantage of (13) is that it yields under some assumptions the existence of a solution to the discrete problem.

Proposition 1. *Assume that the discrete flux Φ_h is given by (13). Assume that the emissivity is constant and that the thermal conductivity is such that $k(T) \geq k_0 > 0$. Then there exists a solution to the discrete problem (11).*

Proof. For simplicity, we assume homogeneous Dirichlet conditions, the general case being treated with additional technical steps. From the renormalization (13) and Gerschgorin's theorem, we deduce that the spectral radius of G is less or equal to one. Let us then establish that $\int_{\Sigma_m} \Phi_h \, T_h \, rdl \geq 0$. In the case where $\varepsilon = 1$, we have $\phi_h = (I - G)b$ and introducing the discrete norms $\|v\| = (\sum_{l=1}^{n_g} \omega_l |v_l|^p)^{1/p}$, $1 \leq p \leq \infty$, we get

$$\begin{aligned}
\int_{\Sigma_m} \Phi_h \, T_h \, rdl &= \sigma \sum_{l=1}^{n_g} \omega_l |T_h(a_l)|^5 - \sum_{l=1}^{n_g} \omega_l (Gb)_l T_h(a_l) \\
&\geq \sigma \|T_h\|_5^5 - \|T_h\|_5 \|Gb\|_{5/4} \\
&\geq \sigma \|T_h\|_5^5 - \|T_h\|_5 \|G\|_{5/4} \|b\|_{5/4} \\
&\geq \sigma (1 - \|G\|_{5/4}) \|T_h\|_5^5 \geq 0,
\end{aligned}$$

since $\|G\|_{5/4}$ is lower than the spectral radius of G. In the case where $\varepsilon < 1$, we may write

$$\Phi_h = Eb - E(I - E)^{-1} \sum_{i=1}^{\infty} (I - E)^i G^i E b$$

with $E = \mathrm{diag}(\varepsilon)$. The series in the rhs is normally convergent and we conclude as before using again $\|G\| \leq 1$. Having established that $\int_{\Sigma_m} \Phi_h \, T_h \, rdl \geq 0$, we deduce an a priori H^1 estimate of the solution T_h by multiplying (11) by T_h and using the coercivity of $\int_{\Omega^T} k(T_h) \nabla T_h \cdot \nabla \Theta_h \, rdrdz$. The existence of a solution to (11) then follows from Brouwer's fixed point theorem. □

Remark. It turns out that in applications with high demands on accuracy, renormalization has a noticeable impact on model predictions. Numerical aspects of renormalization will be investigated in section 4.

3.3 Numerical evaluation of the view matrix

Let x and y be two points in the (r, z) plane with coordinates (r_x, z_x) and (r_y, z_y). Let $m_y(\theta)$ be the point in the physical three-dimensional space obtained with a rotation of angle θ of point y around the symmetry axis. In

order to evaluate the function $f_{axi}(x,y)$ we need to determine the set of angles θ such that $m_y(\theta)$ sees x. For symmetry reasons, it is sufficient to consider $\theta \in [0,\pi]$.

Any point along the ray linking points x and $m_y(\theta)$ can be rotated back to the (r,z) plane. This operation maps the original straight ray in the three-dimensional physical space into a curved hyperbolic ray in the (r,z) plane. The curved ray, denoted by R_θ, is parametrized by

$$t \in [0,1] \mapsto \begin{pmatrix} \sqrt{t^2 r_x^2 + (1-t^2) r_y^2 + 2t(1-t) r_x r_y \cos\theta} \\ t z_x + (1-t) z_y \end{pmatrix}.$$

In axisymmetric configurations, the meridian section of the cavity is simply connected. As a result, the set of $\theta \in [0,\pi]$ such that R_θ lies inside the cavity enclosed by Σ_m is connex (see figure 4). Denoting by $[\theta_{\min}, \theta_{\max}]$ the maximal subset of $[0,\pi]$ such that $\forall \theta \in [\theta_{\min}, \theta_{\max}]$, R_θ lies inside the cavity, we have

$$f_{axi}(x,y) = 2 \int_{\theta_{\min}}^{\theta_{\max}} \mathcal{V}(x, m_y(\theta))\, d\theta. \tag{14}$$

From a computational viewpoint, this approach is attractive because it only involves the *two-dimensional* mesh in the (r,z) plane to solve a three-dimensional shadowing problem.

The evaluation of f_{axi} is based on a ray search method which is performed in three steps:

- *bracketing*: arithmetic sweep of interval $[0,\pi]$ yielding an initial bracketing of the interval $[\theta_{\min}, \theta_{\max}]$;
- *local refinement*: sharp determination of $\theta_{\min}$ and $\theta_{\max}$ using a bisection method;
- *numerical quadrature*: evaluation of f_{axi} as given by (14) using Romberg's quadrature. High accuracy is achieved since $\mathcal{V}(x,y)$ is smooth over the integration interval.

Each curved ray involved in the algorithm is discretized in a finite number of steps whose length is evaluated adaptively as a function of the local mesh triangle that the ray is currently crossing. Several parameters control the numerical performance of the ray search method, realizing a compromise between accuracy and computational cost. This issue will be further investigated in the test cases presented in section 4.

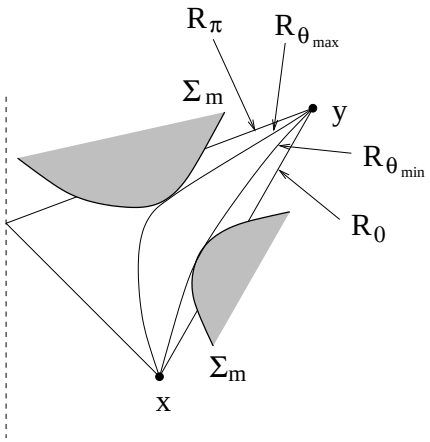

Fig. 4. Curved rays in (r, z) plane and the determination of angles $\theta_{\min}$ and $\theta_{\max}$.

3.4 Fixed point and Newton iteration

The above approximation methods lead to a system of nonlinear equations

$$\begin{cases} \mathcal{L}_A(A_h, T_h) = 0 \\ \mathcal{L}_T(A_h, T_h) = 0 \end{cases}$$

with obvious notation. The thermomagnetic coupling is handled using a fixed point iteration. Given a discrete temperature field T_h^n, we first obtain the magnetic potential from $\mathcal{L}_A(A_h^{n+1}, T_h^n) = 0$ and then update the temperature field from $\mathcal{L}_T(A_h^{n+1}, T_h^{n+1}) = 0$.

The first step in the fixed point method is simply a linear system solved using a GMRes iteration with an ILU preconditionner [14]. The temperature update requires the solution of a nonlinear system of equations using a damped Newton iteration. The Jacobian matrix is evaluated numerically using divided differences. Nonlocal couplings due to radiant energy transfer are fully accounted for in the compressed structure of the matrix. At each Newton step, the linear system is solved approximately using a GMRes iteration with an ILU preconditionner.

4 Numerical results

In this section we present numerical results obtained on three test cases of increasing difficulty.

- Test case 1 consists of a simplified geometric configuration with multiple reflection radiant energy transfer occurring in a single convex cavity. In ad-

dition, electric conductivities are temperature independent thus uncoupling the magnetic potential from the temperature. This test case has been chosen because previous numerical results are available for comparison;
- Test case 2 is the same as test case 1 except that the radiant cavity is now *nonconvex*. The numerical methods used in the approximation of radiant energy transfer are assessed here;
- Test case 3 is a prototype for an industrial growth reactor containing up to 5 radiant cavities (of which 3 are nonconvex).

4.1 Test case 1: convex cavity

The model growth reactor considered in this test case is the one shown in figure 1 except that the induction coils are globally modeled as a rectangular section 0.5 cm wide and 12 cm high. The growth cavity is 2 cm wide and 5 cm high. The thickness of the graphite crucible is 1 cm while that of the insulating foam is 2 cm at its top and bottom and 1 cm laterally. For all materials, the magnetic permeability is that of vacuum $\mu = 4\pi\times10^{-7}$ H/m. Electric conductivities are 2×10^4 in the graphite enclosure, 2×10^3 in the insulating foam and 1×10^4 in the powder (units of $\Omega^{-1}\mathrm{m}^{-1}$). The frequency of the eddy currents is 50 kHz. Two values are considered for the current density: $J_d = 3.128\times10^6$ for test case 1a and $J_d = 4.716\times10^6$ for test case 1b (units of Am^{-2}). The first choice corresponds to Joule losses of 3 kW in the three conducting materials while the second to Joule losses of 3 kW in the graphite. Thermal conductivities are set to 10 for the graphite crucible, 1 for the insulating foam, 25 for the powder and 0.01 for the growth cavity (units of $\mathrm{Wm}^{-1}\mathrm{K}^{-1}$). Emissivities are 0.7 for the crucible, 0.9 for the foam and 0.5 for the powder. Ambient air temperature is set to $T_\infty = 573$ K. The temperature is $T_d = T_\infty$ at the basis of the insulating foam and (6) is imposed elsewhere with the empirical coefficient η set to zero.

We consider four triangulations characterized by an average mesh size h and the truncation radius R (both measured in cm). The maximal value of the Joule dissipation and temperature is presented in table 1. No significant difference is observed among the four calculations showing that the meshes are adequately refined and that the truncation radius R is large enough. A comparison between the results obtained on the finest mesh ($h = 0.1$, $R = 100$) and previous numerical results [2,12] shows excellent agreement. As a further illustration, figure 5 presents contours for the real part of the magnetic potential and the temperature for test case 1a. Figure 6 presents the multiple reflection flux along the meridian Σ_m for test cases 1a and 1b. Note the flux discontinuity at the powder/graphite interface where the emissivity changes value.

mesh				test case 1a		test case 1b	
h	R	np	ne	Joule losses	temperature	Joule losses	temperature
0.2	60	5382	10554	27.61	2459.6	62.75	3291.2
0.1	60	20304	40190	27.93	2461.9	63.50	3296.2
0.2	100	6418	12572	27.65	2462.3	62.85	3295.3
0.1	100	24111	24694	27.98	2464.4	63.59	3300.2
CSC (error in %)				0.9	0.05	0.7	0.1
LTPCM (error in %)				1.0	0.3	1.3	1.2

Table 1
Maximal value of Joule dissipation (MW/m^3) and temperature (K) for test cases 1a and 1b on 4 different meshes; h and R are given in cm while np and ne denote the number of nodes and elements in the mesh; comparison with previous numerical results [2,12].

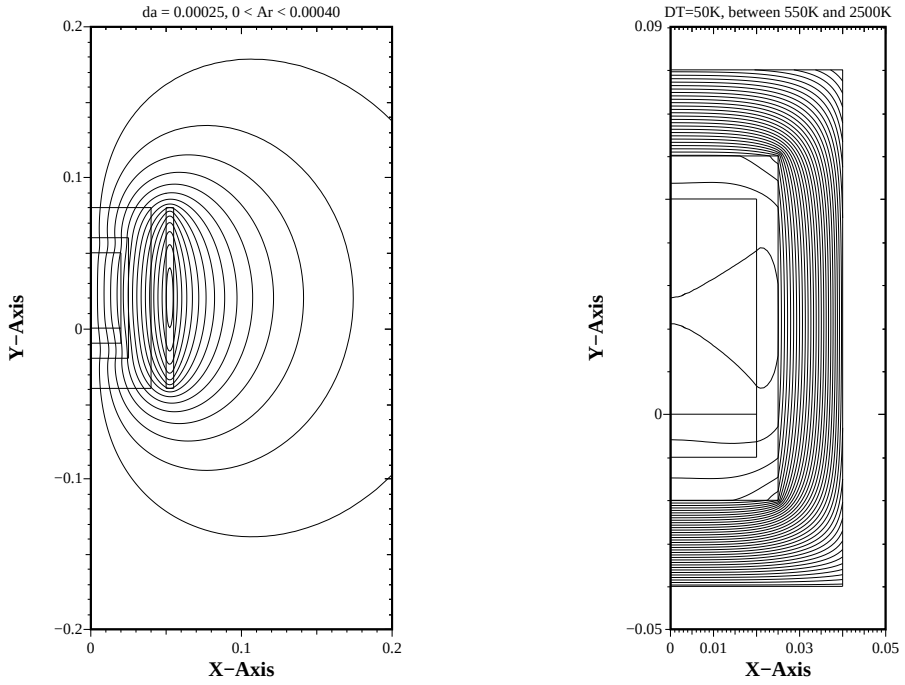

Fig. 5. Test case 1a: contours for real part of magnetic potential (left) and temperature (right).

We next investigate the impact of view matrix renormalization on numerical results. To this purpose, two series of calculations are performed, the first one with renormalization and the second one without. For each series, three meshes are considered: the $(h = 0.2, R = 60)$ mesh, the $(h = 0.1, R = 60)$ mesh, and the $(h = 0.1, R = 60)$ mesh with local refinement near the cavity corners $(h = 0.025)$. Maximum temperatures are reported in table 2 while the temperature distribution as a function of the curvilinear abscissa along Σ_m is

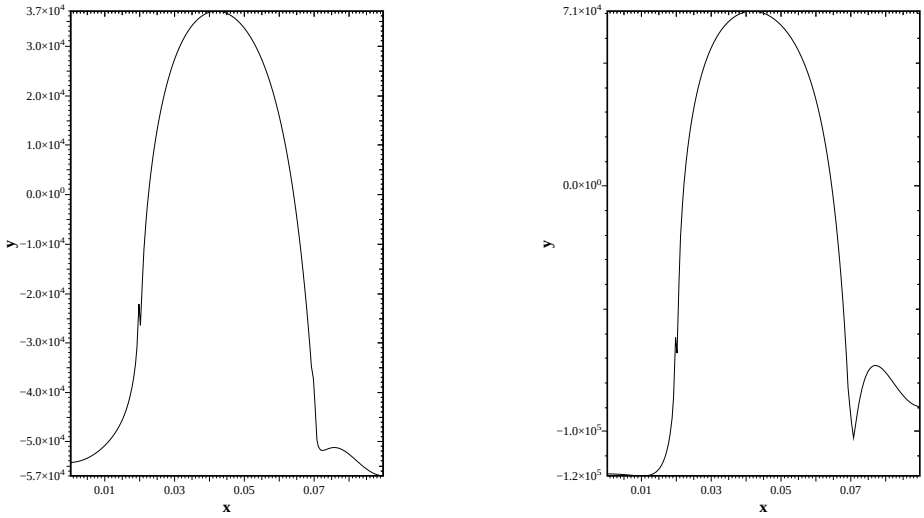

Fig. 6. Multiple reflection flux along meridian Σ_m as a function of curvilinear abscissa starting at the cavity/powder interface at the symmetry axis; test case 1a (left) and 1b (right).

mesh parameters	with	without
$h = 0.2,\ R = 60$	2459.6	2553.8
$h = 0.1,\ R = 60$	2461.9	2504.6
$h = 0.1,\ R = 60$ + corner ref.	2461.8	2472.1

Table 2
Test case 1a: maximum temperature (K) on three different meshes with and without normalization of the view matrix.

reported in figure 7. We observe that without renormalization the numerical results are much more sensitive to mesh refinement and that they converge towards the values obtained with renormalization as the mesh is refined near the corners where singularities arise. The multiple reflection flux is presented in figure 8 as a function of the curvilinear abscissa for the six calculations. Without normalization, the flux exhibits a singularity at the two convex corners. This singularity disappears with normalization.

4.2 Test case 2: nonconvex cavity

Test case 2 is a modified version of test case 1 in which a graphite screen is introduced inside the cavity so that it is no longer convex. The temperature distribution with a zoom near the tip of the screen is presented in figure 9.

As for test case 1, we investigate the impact of view matrix normalization

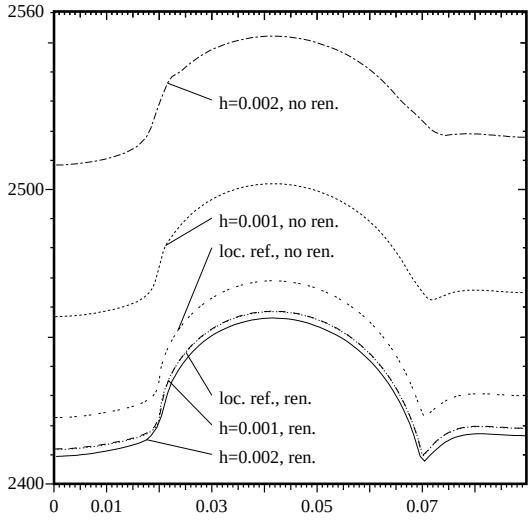

Fig. 7. Test case 1a: temperature distribution along the cavity as a function of curvilinear abscissa.

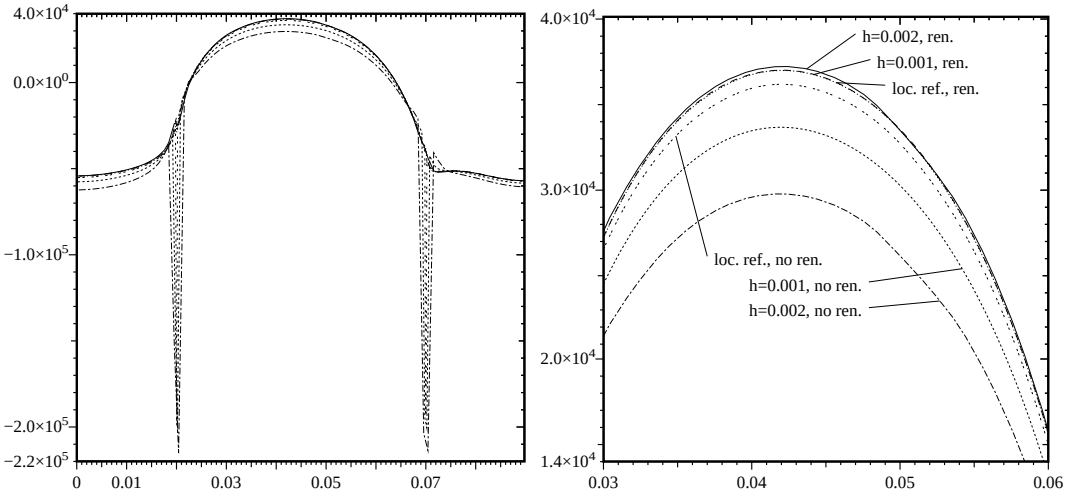

Fig. 8. Test case 1a. Left: multiple reflection flux as a function of curvilinear abscissa s. Right: zoom for $0.03 \leq s \leq 0.06$.

on solution quality. Temperature distribution along the curvilinear abscissa and peak temperatures are reported in figure 10 and table 3 respectively. The multiple reflection flux along the curvilinear abscissa is presented in figure 11. The conclusions drawn for test case 1 are confirmed: without normalization, we observe a high sensitivity to mesh refinement, a singularity of the multiple reflection flux near the convex corners (4 in total) and a nonsingular but inaccurate temperature profile.

As a further investigation of view matrix normalization, we present in figure 12 the quantities $|1 - S_l|$ as a function of curvilinear abscissa. The four singular convex corners are clearly visible. The zoom around a convex corner clearly confirms that no convergence of S_l to unity is observed for the Gauss points

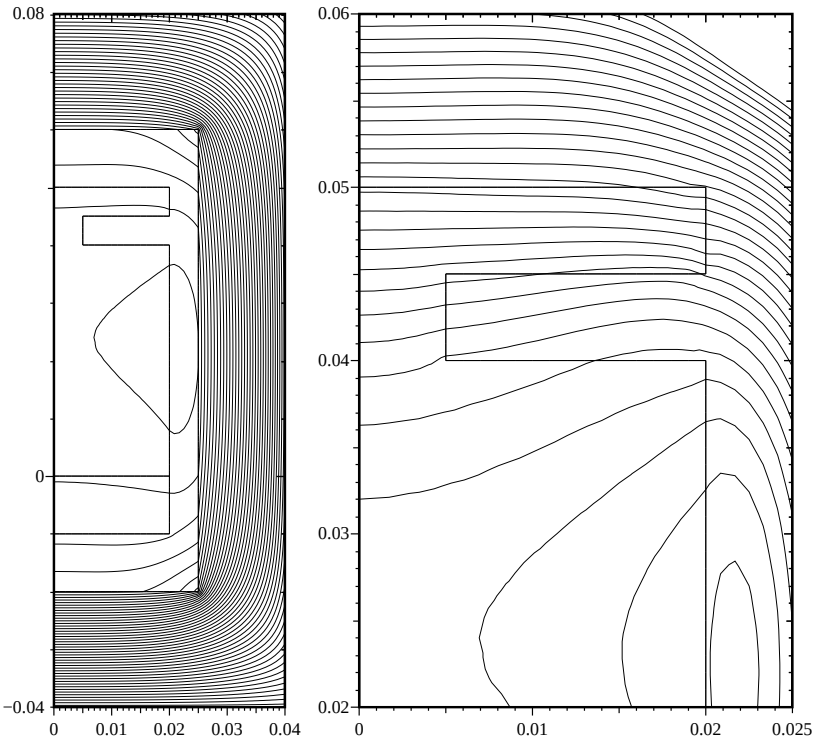

Fig. 9. Test case 2: isotherms. Left: whole domain, $550K \leq T \leq 2500$, $\Delta T = 40K$. Right: zoom around the screen tip, $2350K \leq T \leq 2500$, $\Delta T = 5K$.

mesh parameters	with	without
$h = 0.2$, $R = 100$	2491.4	2730.3
$h = 0.1$, $R = 100$	2492.1	2589.9
$h = 0.1$, $R = 100$ + corner ref.	2492.6	2513.9

Table 3
Test case 2: maximum temperature (K) on three different meshes with and without normalization of the view matrix.

located next to such corners. The zoom near one of the screen tip corners confirms that no singular behavior is obtained. Because of large variations of $\theta_{\min}$ and $\theta_{\max}$ in this region, the deviation of S_l from unity is larger at those corners than at points located inside the cavity edges. The deviation converges to zero almost quadratically when the mesh is refined.

The tradeoff between cost and accuracy in the numerical evaluation of the view matrix is controlled by three numerical parameters :

- n_{ray}: the maximum number of rays in the bracketing step (see section 3.3). Small values of n_{ray} save computational time but may cause the search algorithm to miss small obstacles;
- ϵ_θ: the accuracy of the bisection method for determining $\theta_{\min}$ and $\theta_{\max}$;
- δ: relative step size along ray between obstacle checks; values close to unity

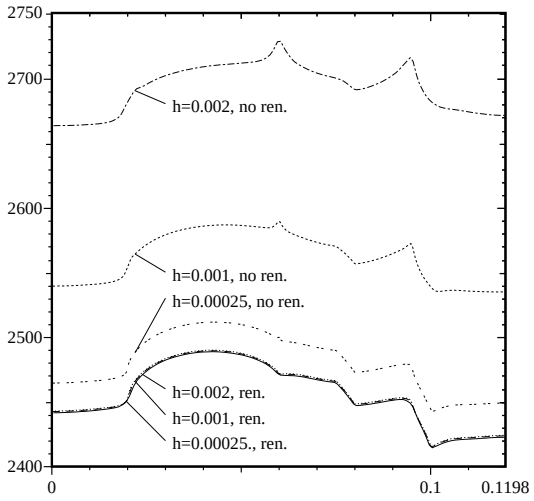

Fig. 10. Test case 2: temperature distribution along the cavity as a function of curvilinear abscissa.

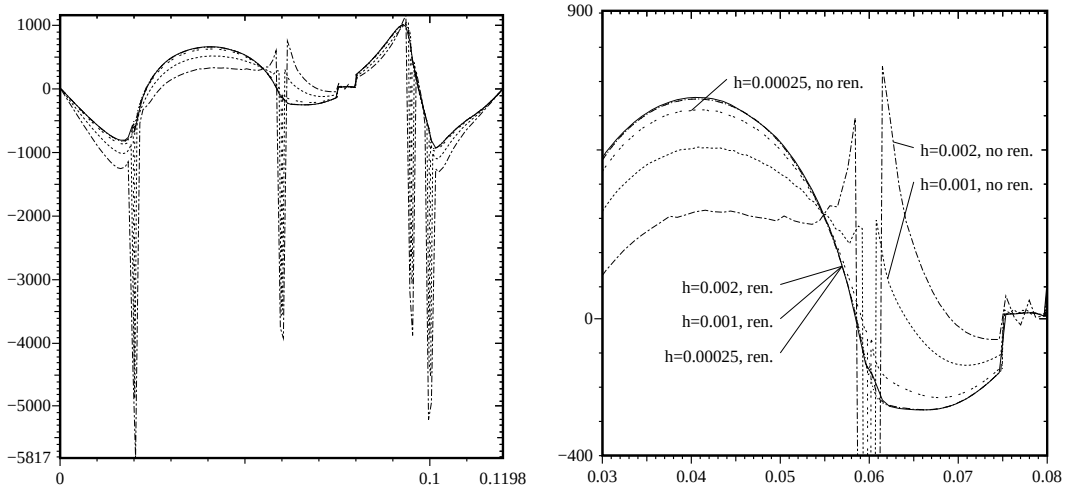

Fig. 11. Test case 2. Left: multiple reflection flux as a function of curvilinear abscissa s. Right: zoom for $0.03 \leq s \leq 0.08$.

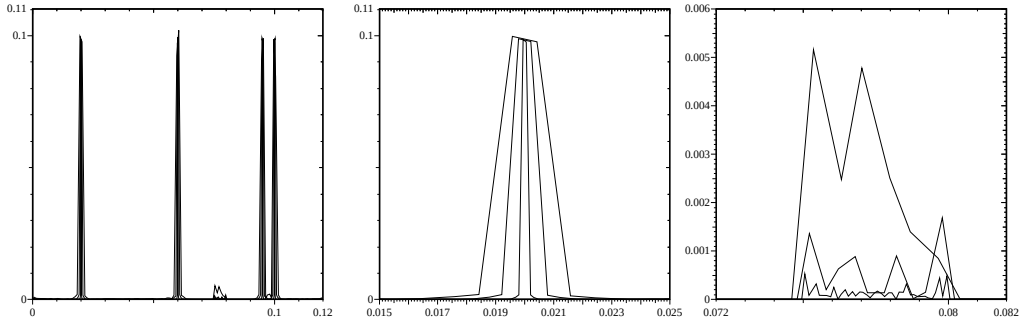

Fig. 12. Error in view matrix normalization as a function of curvilinear abscissa observed on three different meshes. Left: global representation. Center: zoom around the bottom corner $0.015 \leq s \leq 0.025$. Right: zoom around the screen tip, $0.072 \leq s \leq 0.082$.

numerical parameters		speedups	
n_{ray}	ϵ_θ	$\mathcal{S}_1$	$\mathcal{S}_2$
10	10^{-2}	1.34	39
10	10^{-4}	1.34	3318
100	10^{-4}	1.67	506

Table 4
Test case 2: speedups $\mathcal{S}_1$ and $\mathcal{S}_2$ for various numerical strategies in evaluating the view factor matrix.

correspond to step sizes of the order of the local mesh size and may cross small obstacles.

Let n_1 denote the total number of rays considered in the bracketing step and n_2 the total number of rays considered in the local refinement step. Set $n_{tot} = n_1 + n_2$. Then the total cost scales as n_{tot}/δ. We consider the speedups

$$\mathcal{S}_1 = \frac{n_{ray}\, n_g^2}{n_1}, \qquad \mathcal{S}_2 = \frac{\frac{\pi}{\epsilon_\theta}\, n_g^2}{n_{tot}}.$$

$\mathcal{S}_1$ represents the speedup achieved using the connexity of the integration interval with respect to an approach where the whole radiating surface is a priori discretized. $\mathcal{S}_2$ represents the overall speedup with respect to a discretization of the whole radiating surface achieving the same accuracy. These quantities are presented in table 4 for various numerical strategies on the $(h = 0.1, R = 100)$ mesh where $n_g^2 = 57600$. The parameter δ is set to 0.1 in all calculations. The connexity speedup $\mathcal{S}_1$ indicates that a significant amount of computation is saved by first bracketing the interval $[\theta_{\min}, \theta_{\max}]$. The second speedup illustrates the advantage of local refinement when high accuracy is required.

4.3 Test case 3: industrial growth reactor

As an illustration for industrial applications, we finally consider the crystal growth reactor presented in figure 13. The computational domain consists of 15 subdomains of which 5 are multiple reflection radiant cavities: the 2 pyrometric holes (which are convex) and the 3 argon cavities (which are nonconvex). Eddy currents are imposed at an angular velocity of $\omega = 10^5$ rad/s and a current density of $J_d = 1.65{\times}10^6$ A/m^2 yielding a total Joule dissipation in the crucible of 9.86 kW. Electric conductivities are temperature dependent functions given by $\frac{7\times10^4}{3.5\times10^{-4}T+0.375+\frac{144.7}{T}}$ in the graphite crucible, $\frac{400}{3.5\times10^{-4}T+0.375+\frac{144.7}{T}}$ in the insulating foam, and 770 in the SiC powder and seed (units of $\Omega^{-1}\mathrm{m}^{-1}$, T given in Celsius) [11]. The thermal conductivity is also temperature dependent and given by $\frac{120}{1+2\times10^{-3}T}$ in the graphite crucible, $0.17{\times}10^{-6}T^2 + 0.08$ in

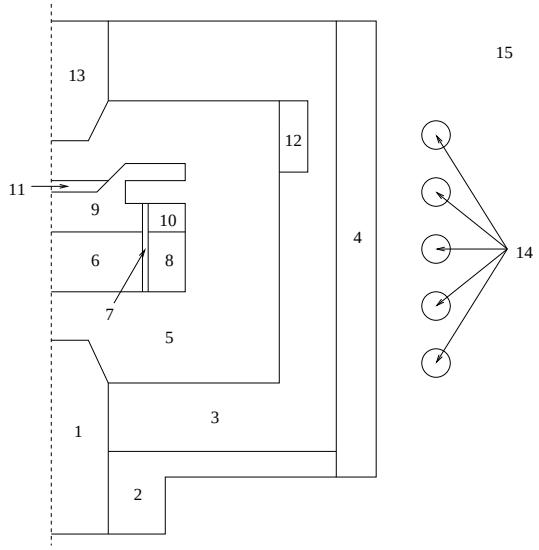

Fig. 13. Schematics of an industrial prototype reactor (not in scale); 1: lower pyrometric hole, 2: graphite lid, 3: insulating foam, 4: water-cooled quartz tube, 5: graphite crucible, 6: first SiC powder reservoir, 7: graphite ring, 8: second SiC powder reservoir, 9: primary argon cavity where growth occurs, 10: second argon cavity, 11: SiC seed, 12: third argon cavity, 13: upper pyrometric hole, 14: induction coils, 15: ambient air.

the insulating foam, $0.51\times10^{-2} + 0.454\times10^{-4}T - 0.944\times10^{-8}T^2$ in the argon cavities, 2 in the quartz and SiC powder, and 10 in the SiC seed (units of $\mathrm{Wm}^{-1}\mathrm{K}^{-1}$, T again given in Celsius). The emissivities of radiating materials are set to 0.9. On the outer boundary of the quartz tube, the temperature is set to $T_d = 300$ K while an homogeneous Neumann condition is imposed at the bottom and top of the quartz tube. On the boundaries corresponding to the insulating foam and the graphite lid, (6) is used with the empirical coefficient η set to 10 and an ambient air temperature of $T_\infty = 300$ K. The lower and upper pyrometric holes are open radiating cavities which are modeled by adding an artificial boundary at temperature T_∞.

Numerical results are presented in figure 14. The mesh extends to $R = 1$ m. The mesh size is around $h = 0.3$ cm in most parts of the reactor descending down to 0.03 cm in the SiC seed. Temperature peaks in the graphite crucible close to the SiC powder reservoirs. We also note that a fairly vertical temperature gradient is achieved inside the primary argon cavity. For these type of problems, 5 fixed point iterations are required to handle the thermomagnetic coupling and less than 10 Newton iterations to cope with the nonlinearities in radiant energy transfer. Finally, we point out that for this problem, peak temperatures would be up to 400 K higher if the view matrix was not normalized. This numerical evidence further supports the theoretical importance of renormalization.

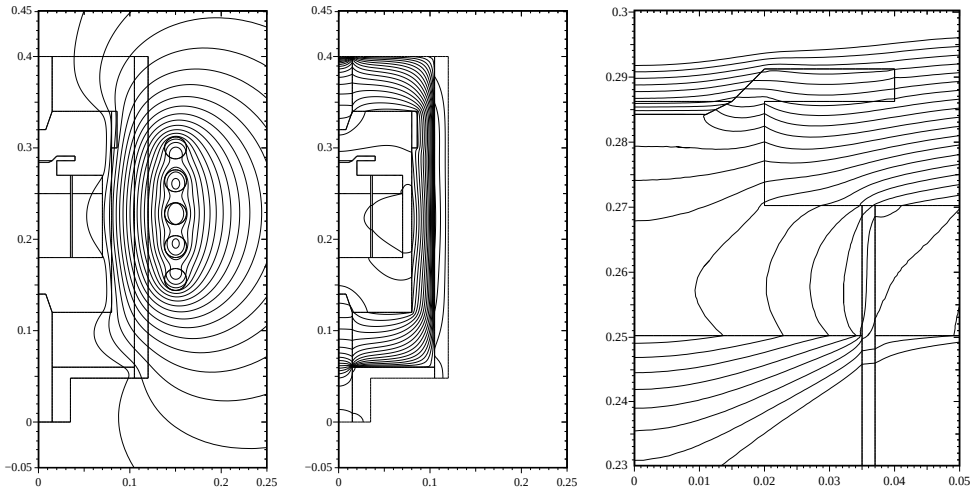

Fig. 14. Prototype for an industrial growth reactor: isopleths for real part of magnetic potential (left), isotherms for the whole reactor (middle) and zoom around crystal seed (right).

5 Conclusions

We have investigated a thermomagnetic problem with multiple reflection radiant energy transfer arising in crystal growth reactors. The governing equations consist of three PDEs coupled with a nonlinear integral equation. The numerical methodology derived in this paper relies on a discontinuous Galerkin approximation to the integral equation and uses a local refinement strategy in the azimuthal direction around shadowing obstacles. Furthermore, a renormalization of the view factor matrix is introduced in order to cope with singularities at Gauss nodes near convex corners. The present thermomagnetic model allows for an accurate and robust evaluation of the temperature field around the crystal seed and is now ready to be embedded in more comprehensive models of the growth process accounting for multicomponent mass transfer in the gas phase, surface reactivity at the moving gas/crystal interface and defect incorporation due to thermal stresses.

Acknowledgment. The authors are thankful to M. Pons, J.-M. Dedulle and R. Madar (LTPCM, INPG) for stimulating discussions and partial support.

References

[1] Q.-S. Chen, H. Zhang, and V. Prasad. Heat transfer and kinetics of bulk growth of silicon carbide. *J. Crystal Growth*, 230:239–246, 2001.

[2] J.-M. Dedulle. Modélisation magnéto-thermique du creuset d'élaboration SiC.

internal report, LTPCM, INPG.

[3] D. Hofmann, M. Heinze, A. Winnacker, F. Durst, L. Kadinski, P. Kaufmann, Yu. Makarov, and M. Schäfer. On the sublimation growth of SiC bulk crystals: development of a numerical process model. *J. Crystal Growth*, 146:214–219, 1995.

[4] J.P. Holman. *Heat Transfer*. McGraw-Hill, New York, 7th edition, 1990.

[5] J.R. Howell. *Configuration factors*. McGraw-Hill, New York, 1982.

[6] L. Kadinski and M. Perić. Numerical study of grey-body surface radiation coupled with fluid flow for general geometries using a finite volume multigrid solver. *Int. J. Num. Meth. Fluid Flow*, 6:3–18, 1996.

[7] A.V. Kulik, S.E. Demina, S.K. Kochuguev, D.Kh. Ofengeim, S.Yu. Karpov, A.N. Vorob'ev, M.V. Bogdanov, and M.S. Ramm. Inverse-computation design of a SiC bulk crystal growth system. *Mat. Res. Soc. Symp. Proc.*, 640:H1.6.1–H1.6.6, 2001.

[8] J. Monnier and J.P. Vila. Convective and radiative thermal transfer with multiple reflections. Analysis and approximation by a finite element method. *Math. Mod. Meth. Appl. Sci.*, 11(2):229–262, 2001.

[9] C. Perret and P. Witomski. Equation de la chaleur et réflections multiples. *Ann. Inst. Henri Poincaré*, 8(6):677–689, 1991.

[10] M. Pons, M. Anikin, K. Chourou, J.-M. Dedulle, R. Madar, E. Blanquet, A. Pisch, C. Bernard, P. Grosse, C. Faure, G. Basset, and Y. Grange. State of the art in the modelling of SiC sublimation growth. *Mater. Sci. Eng.*, B61–62:18–28, 1999.

[11] M. Pons, E. Blanquet, J.-M. Dedulle, I. Garcon, R. Madar, and C. Bernard. Thermodynamic heat transfer and mass transport modeling of the sublimation growth of silicon carbide crystals. *J. Electrochem. Soc.*, 143(11):3727–3735, 1996.

[12] P. Råback. *Modeling of the sublimation growth of silicon carbide crystals*. PhD thesis, Helsinki University of Technology, Center for Scientific Research, Espoo, 1999.

[13] M.S. Ramm, E.N. Mokhov, S.E. Demina, M.G. Ramm, A.D. Roenkov, Yu.a. Vodakov, A.S. Segal, A.N. Vorob'ev, S.Yu. Karpov, A.V. Kulik, and Yu.N. Makarov. Optimization of sublimation of SiC bulk crystals using modeling. *Mat. Sci. Eng.*, B61–62:107–112, 1999.

[14] Y. Saad. *Iterative methods for sparse linear systems*. PWS Publishing Company, Boston, 1996.

[15] M.G. Saldanha de Gama. An alternative mathematical modelling for coupled conduction/radiation energy transfer phenomenon in a system of N grey bodies surrounded by a vacuum. *Int. J. Non-Linear Mech.*, 30(4):433–447, 1995.

[16] M. Selder, L. Kadinski, F. Durst, and D. Hofmann. Global modeling of SiC sublimation growth process: prediction of thermoelastic stress and control of growth conditions. *J. Crystal Growth*, 226:501–510, 2001.

[17] M. Selder, L. Kadinski, F. Durst, T. Straubinger, and D. Hofmann. Numerical simulation of global heat transfer in reactors for SiC bulk crystal growth by physical vapor transport. *Mater. Sci. Eng.*, B61–62:93–97, 1999.

[18] Yu.M. Tairov and V.F. Tsvetkov. General principles of growing large size single crystals of various silicon carbide polytypes. *J. Crystal Growth*, 52:146–150, 1981.

[19] T. Tiihonen. A nonlocal problem arising from heat radiation on non-convex surfaces. *Euro. J. Appl. Math.*, 8:403–416, 1997.

[20] T. Tiihonen. Stefan-Boltzmann radiation on non-convex surfaces. *Math. Methods Appl. Sci.*, 20:47–57, 1997.

[21] P.J. Wellmann, D. Hofmann, L. Kadinski, M. Selder, T.L. Straubinger, and A. Winnacker. Impact of source material on silicon carbide vapor transport growth process. *J. Crystal Growth*, 225:312–316, 2001.